

# A 2.5D numerical study on open water hydrodynamic performance of a Voith-Schneider propeller

Mohammad Bakhtiari and Hassan Ghassemi\*

Department of Maritime Engineering, Amirkabir University of Technology, Tehran, Iran

Received: 15 September 2018 / Accepted: 20 September 2019

**Abstract.** Marine cycloidal propeller (MCP) is a special type of marine propulsors that provides high maneuverability for marine vessels. In a MCP, the propeller axis of rotation is perpendicular to the direction of thrust force. It consists of a number of lifting blade. Each blade rotates about the propeller axis and simultaneously pitches about its own axis. The magnitude and direction of thrust force can be adjusted by controlling the propeller pitch. Voith-Schneider propeller (VSP) is a low-pitch MCP with pure cycloidal blade motion allowing fast, accurate, and stepless control of thrust magnitude and direction. Generally, low-pitch cycloidal propellers are used in applications with low speed maneuvering requirements, such as tugboats, minesweepers, etc. In this study, a 2.5D numerical method based on unsteady RANS equations with SST  $k-\omega$  turbulent model was implemented to predict the open water hydrodynamic performance of a VSP for different propeller pitches and blade thicknesses. The numerical method was validated against the experimental data before applying to VSP. The results showed that maximum open water efficiency of a VSP is enhanced by increasing the propeller pitch. Furthermore, the effect of blade thickness on open water efficiency is different at various advance coefficients, so that the maximum efficiency produced by the VSP decreases with increasing blade thickness at different propeller pitches.

**Keywords:** Voith-Schneider propeller / low-pitch / pure cycloidal motion / 2.5D numerical method / blade thickness effect

## 1 Introduction

Marine propulsion is an important engineering issue with a long history. Until the 1970s, the conventional screw propeller has shown a superior performance among the modes of marine propulsion. With the development of special purpose ship types in the last decades, a well-balanced compromise is demanded between the main requirements of ship propulsion, such as high efficiency, minimum cavitation, noise and erosion, high maneuverability and minimum vulnerability and low maintenance costs. Modern screw propellers have shown to be competitive to the conventional screw propeller. Although screw propellers offer several advantages, such as mechanical simplicity, they have some practical limitations in increasing overall hydrodynamic efficiency, such as the limitations of aspect ratio due to cavitation at high tip speeds [1,2]. Cycloidal propellers are promising alternative concepts to screw propellers. The idea of cycloidal propeller dates back to the early 1870s. One of the important

distinguishing features of a cycloidal propeller is that the axis of rotation is perpendicular to the thrust force, as opposed to a screw propeller, in which the axis of rotation is along the thrust force. Cycloidal propellers are also known as vertical-axis propellers. A marine cycloidal propeller consists of a number of lifting blades fitted to a disc usually set flush with the ship hull. The disc revolves about the vertical axis (propeller axis of rotation) while the blades oscillate about their own individual axes through a mechanical linkage system, as shown in Figure 1. In this type of propulsor system, the propulsion and manoeuvring units are combined together as a single unit. Therefore, no separate rudder is required to manoeuvre the ship.

So far, two configurations have been studied and developed based on pitch propeller for this type of marine propellers. First configuration is a low-pitch propeller (designed for advance coefficient less than one, means  $\lambda < 1$ ) referred as cycloidal propellers, and second one is a high-pitch propeller (designed for  $\lambda > 1$ ) referred as trochoidal propellers. Blade trajectories for  $\lambda < 1$  and  $\lambda > 1$  are shown in Figure 2.  $\lambda$  is absolute advance coefficient of marine cycloidal propeller and defined as  $V_A/R\omega$ , where  $V_A$ ,  $\omega$  and  $R$  are advance velocity, angular velocity and radius of the propeller, respectively.

\* e-mail: [gasemi@aut.ac.ir](mailto:gasemi@aut.ac.ir)



**Fig. 1.** (a) Top view of a cycloidal propeller with 6 blades. (b) Ship with twin cycloidal propellers.

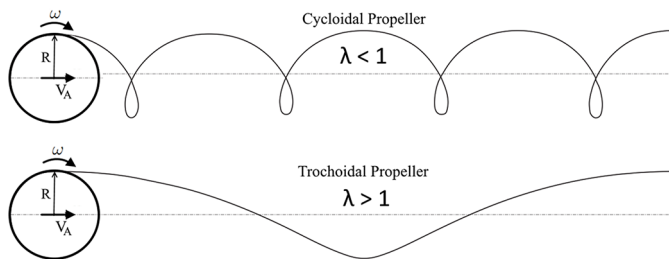


**Fig. 2.** Different blade trajectories of cycloidal propellers.

High-pitch propellers provide higher hydrodynamic efficiency than low-pitch propellers and permit high-speed operation. However, low-speed maneuvering requirements have led to further development of the low-pitch configuration. Voith-Schneider propeller is a well-known commercial application of a low-pitch cycloidal propeller optimized for high rotation speed and high thrust production. It is used primarily for ships that have to satisfy particularly demanding safety and manoeuvrability requirements. The VSP has very rapid and precise thrust variation according to Cartesian Coordinates and it makes the VSP an ideal propulsion system for efficient dynamic positioning even in extremely rough weather conditions [3].

Although the idea of cycloidal propeller was originated over a century ago, rigorous theoretical analyses and systematic experiments were performed much later. Kirsten was the first person who worked on a fixed low-pitch cycloidal propeller in 1922 [4]. In 1928, Schneider improved Kirsten's design by creating a variable low-pitch device and commercialized his design under the name Voith-Schneider propeller (VSP) [5,6]. Henry provided a survey of marine cycloidal propeller in 1959, which was a foundation for subsequent theoretical analyses and systematic series of experiments [7]. Early theoretical models presented for analyzing marine cycloidal propeller made simplifying assumptions, leading to inaccurate models [8]. Also, most theoretical models were developed in 2D, neglecting 3D effects. In 1961, Haberman and Harley used

Taniguchi's method [8] for calculating the hydrodynamic performance of a cycloidal propeller with semi-elliptical blades [9]. In later years, improvements in performance of cycloidal propeller were presented by Sparenberg and James, [10–12]; Sparenberg optimized the blade pitch function of a single-blade propeller by minimizing kinetic energy in the wake of 1969, and James worked on Sparenberg's optimization work with a more detailed model in 1971. Much later, in 1991, Brockett created a computational model employing lifting line and actuator disk theories in an attempt to optimize the pitch function [13]. Van Manen and Van Terwisga expanded Brockett's computational model to optimize the pitch function [14].

In most experimental tests of marine cycloidal propeller, blades with small aspect ratios have been used leading to poor agreement with theoretical models. Systematic series of these experiments were carried out by Nakonechny [15,16], Van Manen [17], Ficken [18], Bjarne [19], and Bose and Lai [20]; Van Manen's systematic tests showed lower hydrodynamic efficiency for low-pitch propellers relative to high-pitch propellers. Furthermore, Van Manen demonstrated that Sparenberg's pitch function is more efficient than a cycloidal pitch function for multi-bladed propellers.

More recently, using computational fluid dynamics (CFD) to analyze marine cycloidal propeller have been extended [21–25]. Extensive studies have been carried out on Voith-Schneider propeller (VSP) as a low-pitch cycloidal marine propeller by Jurgens et al. In 2005, Jurgens et al. presented a numerical optimization of blade steering curve for Voith-Schneider propeller by using CFD method [21]. Various profiles of VSP blades have been investigated in tests with single-bladed model and in propulsion and cavitation tests with VWT model. The results of these tests have been presented at the Hydrodynamic Symposium – Voith Schneider Propulsion in 2006 [26]. In later years, Jurgens et al. investigated the influence of the VSP on stern slamming conditions, the roll damping capabilities of the VSP and the effect of air ventilation. They used experimental and CFD methods and compared the results of VSP with azimuth thruster. They demonstrated that the VSP decreases the impact of

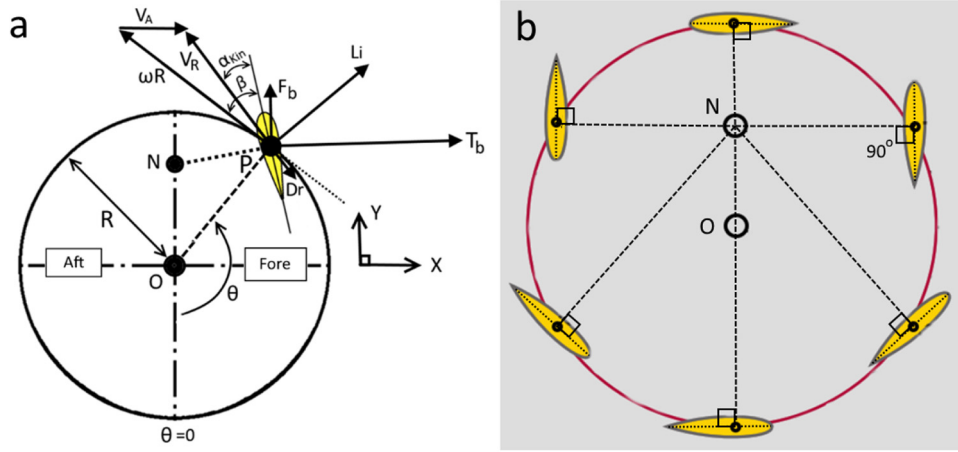


Fig. 3. (a) Kinematics of a cycloidal propeller. (b) Schematic of a 6-bladed VSP.

stern slamming pressure because of its vertical rotating axis, and can be used to reduce the roll motion of a vessel. They also showed that VSP is less prone to ventilation than azimuth thruster [23,24]. At the same year, Jurgens and Heinke investigated cavitation behaviour of heavily loaded VSP with different blade profiles under bollard pull condition [27].

In the present study, the open water hydrodynamic performance of a Voith-Schneider propeller (a low-pitch marine cycloidal propeller with pure cycloidal blade motion) is studied at different propeller pitches. Also, the effect of blade thickness on hydrodynamic performance is investigated. For this purpose, a 2.5D numerical model is implemented in which the 3D unsteady RANS equations coupled with SST  $k-\omega$  turbulent model are solved in a computational domain with one-chord length in spanwise direction for including necessary 3D effects. The Ansys Fluent code is used to solve the equations. The computations are performed for a 4-bladed VSP, including blades with uniform section profile of symmetric NACA 4-digits airfoil. Before applying to investigate the VSP performance, the numerical model is validated against experimental data.

## 2 Hydrodynamic principles governing the performance of a VSP

The kinematics of a marine cycloidal propeller is primarily defined by absolute advance coefficient, which is the ratio of propeller advance velocity to blade circumferential velocity:

$$\lambda = \frac{V_A}{\omega R}, \quad (1)$$

where,  $V_A$ ,  $\omega$  and  $R$  are advance velocity, angular velocity and radius of the propeller, respectively. Kinematics of a cycloidal propeller for one blade have been shown in Figure 3a. In this figure,  $\theta$  is angle of rotation,  $\beta$  is blade pitch angle (the angle between blade chord line and tangent line to rotation circle) and is kinematic angle of attack.

$Li$  and  $D_r$  are hydrodynamic forces of drag and lift producing thrust and side forces of  $T_b$  and  $F_b$  acting on one blade.  $V_R$  is the resultant velocity of blade due to propeller advance and rotation.

In a cycloidal propellers, blade pitch angle ( $\beta$ ) can be considered as the second important parameter defining the kinematics of the propeller, since it ultimately dictates kinematic angle of attack, and thus the resulting hydrodynamic loads on the propeller blade.

As mentioned before, Voith-Schneider propeller (VSP) is low-pitch cycloidal propeller. In a VSP, the blade pitch angle changes in such a way that the normal to the chord line at blade axis of rotation (point P in Fig. 3a) passes through a fixed point, called the steering center (point N in Fig. 3). The pitch angles of the blades for a 6-bladed VSP at a moment for a specified value of ON (eccentricity) are illustrated in Figure 3b. As can be seen, the perpendiculars to chord lines of the blades intersect at a single point, N. So, the blade pitch angle for a VSP propeller may be stated as a function of  $\theta$  and  $e$ :

$$\beta(\theta, e) = \tan^{-1} \left( \frac{e \sin \theta}{1 + e \cos \theta} \right), \quad (2)$$

where,  $e$  is eccentricity or pitch of a VSP defined as:

$$e = \frac{ON}{R}. \quad (3)$$

In practice, due to mechanical constraints and high pitch rate of blade near  $\theta = \pi$ , the pitch of a VSP can be varied within range  $\leq 0.8$ . The blade motion described by equation (2) is referred as pure cycloidal motion, which is shown in Figure 4 for different pitches of a VSP. The pitch rate of the blade is also shown in Figure 5 for different propeller pitches. It can be seen that, by increasing the propeller pitch, the pitch rate of the blade near  $\theta = \pi$  increases extremely.

The total side force, thrust and torque of a VSP are the sum of forces and moments produced by all blades of the propeller at each time. The side force is significantly lower than the thrust force, because the side forces produced by

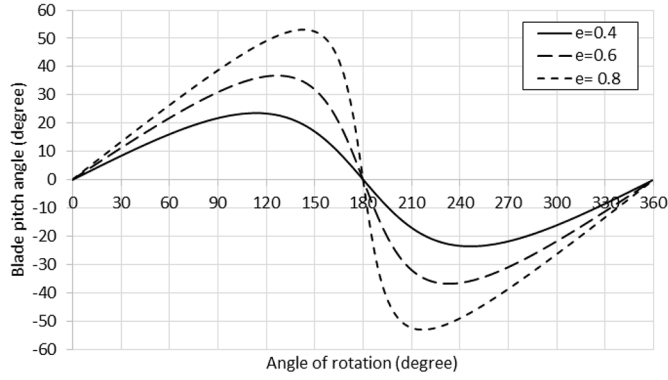


**Fig. 4.** Diagram of blade pitch angle for different pitches of a VSP.

blade at the fore and aft part of the propeller are in the opposite directions and nearly cancel each other, whereas the thrust forces are in the same directions and supplement each other. The unsteady thrust and torque are averaged over one revolution of propeller to obtain the averaged value of thrust ( $T_{ave}$ ) and torque ( $Q_{ave}$ ), and consequently, the open water hydrodynamic characteristics of a VSP are defined as:

$$K_s = \frac{T_{ave}}{\frac{1}{2}\rho D L u^2} \quad (4)$$

$$K_d = \frac{2Q_{ave}}{\frac{1}{2}\rho D^2 L u^2} \quad (5)$$

$$\text{Eff} = \frac{K_s}{K_d} \lambda, \quad (6)$$

where,  $T_{ave}$ ,  $Q_{ave}$ ,  $K_s$ ,  $K_d$  and Eff are average thrust, average torque, thrust coefficient, torque coefficient and open water efficiency of a VSP, respectively.  $D$  and  $L$  are propeller diameter and blade span length, and  $u = \omega R$  is circumferential velocity of the blade.

### 3 Numerical model

In a Voith-Schneider propeller, the hydrofoil blades are exposed to high kinematic angles of attack, sometimes beyond the dynamic stall angle [13]. So, the flow on the blades is three dimensional (3D), highly separated and unsteady [28]. The 3D effects in spanwise directions of the blades cannot be included in a 2D CFD simulation. Quasi-3D or full 3D simulation can be adopted to overcome the shortcomings of a 2D model. In Quasi-3D CFD simulation approach, the 2D model is extended in a spanwise direction for a considerable length in order to resolve the effects of the flow in the 3rd dimension, with periodic boundary conditions at two extremities of the domain. Since, the spanwise length is not fully modeled; it is referred to as 2.5D CFD simulation in order to differentiate it from 2D

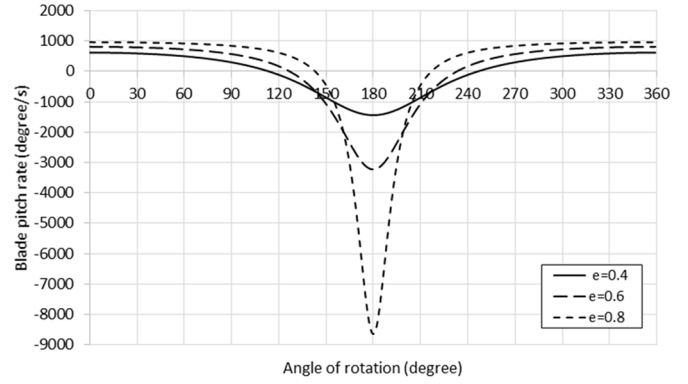


**Fig. 5.** Diagram of blade pitch rate for different propeller pitches of a VSP.

and full 3D simulations of a VSP. Gao et al. performed 2.5D CFD simulations of the flow around a single airfoil and demonstrated that the 2D model is not adequate for predicting the unsteady flow with large separations around airfoils at relatively high angles of attack [29].

According to the abovementioned issues as well as the high computational cost for full 3D simulations of a VSP, a 2.5D CFD approach is implemented here to investigate the hydrodynamic performance of a VSP at different operating conditions for different propeller pitches and blade thicknesses. The unsteady 3D RANS equations with SST  $k-\omega$  turbulent model are used as governing equations. The equations are solved numerically in a solution domain with one-chord length in spanwise direction by using Ansys Fluent code. The SIMPLE scheme is used for pressure-velocity coupling. In addition, the second-order upwind and second-order implicit schemes are implemented for spatial and temporal discretizations of the equations, respectively. Also, the solution domain is discretized by polyhedral cells. This study is carried out for a 4-bladed VSP including blades with uniform section profile of symmetric NACA 4-digits airfoil. Since, the effects of the blade tip cannot be included in a 2.5D simulation, the results of these calculations can only be used for VSP propellers with high aspect ratio (Span-to-Chord ratio of the blade), in which the tip effects on hydrodynamic forces are negligible. The details of the numerical method are provided in the next sections.

#### 3.1 Governing equations

The governing equations of a fluid flow are Navier–Stokes equations. For a turbulent flow, by time-averaging the Navier–Stokes equations, the unsteady Reynolds-averaged Navier–Stokes (URANS) equations are obtained as:

$$\frac{\partial u_i}{\partial x_i} = 0, \quad (7)$$

$$\frac{\partial}{\partial t}(\rho u_i) + \frac{\partial}{\partial x_j}(\rho u_i u_j) = -\frac{\partial p}{\partial x_i} + \frac{\partial}{\partial x_j} \left[ \mu \frac{\partial u_i}{\partial x_j} - \overline{\rho u'_i u'_j} \right] + g_i, \quad (8)$$

where,  $u$  and  $p$  are velocity and pressure, respectively.  $\rho$  and  $\mu$  are fluid density and viscosity, respectively, and  $g$  is gravity force.

Reynolds stresses,  $-\overline{\rho u'_i u'_j}$ , in equation (2) are modeled by using Boussinesq hypothesis that relates the Reynolds stresses to the mean velocity gradients as follows:

$$-\overline{\rho u'_i u'_j} = \mu_t \left( \frac{\partial u_i}{\partial x_j} + \frac{\partial u_j}{\partial x_i} \right) - \frac{2}{3} \left( \rho k + \mu_t \frac{\partial u_k}{\partial x_k} \right) \delta_{ij}, \quad (9)$$

where,  $\mu_t$  is turbulent viscosity.

Here, the two-equation Shear-Stress Transport (SST)  $k$ - $\omega$  turbulence model is used for modeling turbulent viscosity. This model was developed by Menter [30] to effectively blend the robust and accurate formulation of the  $k$ - $\omega$  model in the near-wall region with the free stream independence of the  $k$ - $\epsilon$  model in the far field. A brief overview of this model is given below (for more details, see [30]).

In SST  $k$ - $\omega$  turbulence model, the turbulent viscosity,  $\mu_t$ , is computed as follows:

$$\mu_t = \frac{\rho k}{\omega} \frac{1}{\max \left[ \frac{1}{\alpha^*}, \frac{SF_2}{\alpha_1 \omega} \right]}, \quad (10)$$

where,  $k$  and  $\omega$  are turbulence kinetic energy and specific dissipation rate, respectively, obtained from the following transport equations:

$$\frac{\partial}{\partial t}(\rho k) + \frac{\partial}{\partial x_i}(\rho k u_i) = \frac{\partial}{\partial x_j} \left[ \left( \mu + \frac{\mu_t}{\sigma_k} \right) \frac{\partial k}{\partial x_j} \right] + G_k - \rho \beta^* k \omega \quad (11)$$

$$\frac{\partial}{\partial t}(\rho \omega) + \frac{\partial}{\partial x_j}(\rho \omega u_j) = \frac{\partial}{\partial x_j} \left[ \left( \mu + \frac{\mu_t}{\sigma_\omega} \right) \frac{\partial \omega}{\partial x_j} \right] + G_\omega - \rho \beta \omega^2 + D_\omega, \quad (12)$$

where,  $G_k$  and  $G_\omega$  are generation of  $k$  and  $\omega$  respectively.  $\sigma_k$  and  $\sigma_\omega$  are the turbulent Prandtl numbers for  $k$  and  $\omega$ :

$$\sigma_k = \frac{1}{F_1/\sigma_{k,1} + (1 - F_1)/\sigma_{k,2}}, \quad (13)$$

$$\sigma_\omega = \frac{1}{F_1/\sigma_{\omega,1} + (1 - F_1)/\sigma_{\omega,2}}. \quad (14)$$

In above equations,  $F_1$  and  $F_2$  are blending functions.

### 3.2 Solution domain and boundary conditions

As described in previous sections, kinematics of a Voith-Schneider propeller is such that two rotational motions can be defined for the propeller blade; a constant angular velocity of  $\omega$  due to propeller rotation about its axis (point O in Fig. 3), and a time-dependent angular velocity of  $\dot{\beta}(\theta, \omega, e)$  due to pitching motion of the blade about its own axis (point P in Fig. 3). Accordingly, the blades are

considered as moving walls with angular velocities of  $\omega$  and  $\dot{\beta}$  about O and P (refer to Fig. 3) respectively. Therefore, a number of moving zones (zones 1, 2, 3 and 4 in Fig. 6) are defined around each blade, which rotate at the same velocity as the blade. A moving zone (zone 5 in Fig. 6) is defined around all propeller blades, which rotates at the same velocity as the propeller, and a fixed zone (zone 6 in Fig. 6) at far field. Different zones of the solution domain, as well as applied boundary conditions are shown in Figure 6. In this figure,  $D$  is blade orbit diameter and  $c$  is blade chord length. A translational periodic boundary condition is used for the top and bottom boundaries of each zone. The interface boundary condition is applied to the contact surfaces of the zones. By discretizing each zone by an independent mesh, a cell zone is created. During the transient calculations, each cell zone slides (i.e., rotates at desired angular velocity) relative to one another along the mesh interface. Therefore, no mesh deformation occurs within any zones.

### 3.3 Computational mesh

An unstructured polyhedral mesh is employed to discretize the solution domain around VSP propeller. This type of mesh, introduced by some well-known CFD merchant codes as an innovative approach, combines the advantages of structured hexahedral mesh (low numerical diffusion resulting in accurate solution) and tetrahedral mesh (rapid automatic generation) as well as to overcome the disadvantages of both the above mentioned types of meshes (such as, being time-consuming and sensitive to stretching). The major advantage of a polyhedral mesh is that each polyhedral cell has many neighbors, so gradients can approximate more accurate than structured hexahedral and unstructured tetrahedral meshes. In some cases, polyhedral mesh can even achieve better accuracy than structured hexahedral meshes due to larger number of neighboring cells. Some studies have verified that with polyhedral meshes, one need about four times fewer cells, half the memory and a tenth to fifth of computing time compared to tetrahedral meshes to reach solutions of the same accuracy. In addition, convergence properties are much better in computations on polyhedral meshes, where the default solver parameters usually do not need to be adjusted [31]. Peric [32] presented a more detailed study on properties of different mesh types.

A detailed view of the mesh generated in different zones of the solution domain is illustrated in Figure 7. This figure relates to the finest mesh used in calculation after mesh independence study. As shown in this figure, the meshes of zones 1, 2, 3 and 4 are the same. An inflation polyhedral layer mesh including 45 layers with growth rate of 1.1 and  $Y^+ < 1$  ( $Y^+$  is nondimensional distance of the first layer from the wall) was used within near-wall region.

## 4 Verification and validation of the numerical model

In this section, the accuracy of presented numerical model in predicting open water characteristics of a

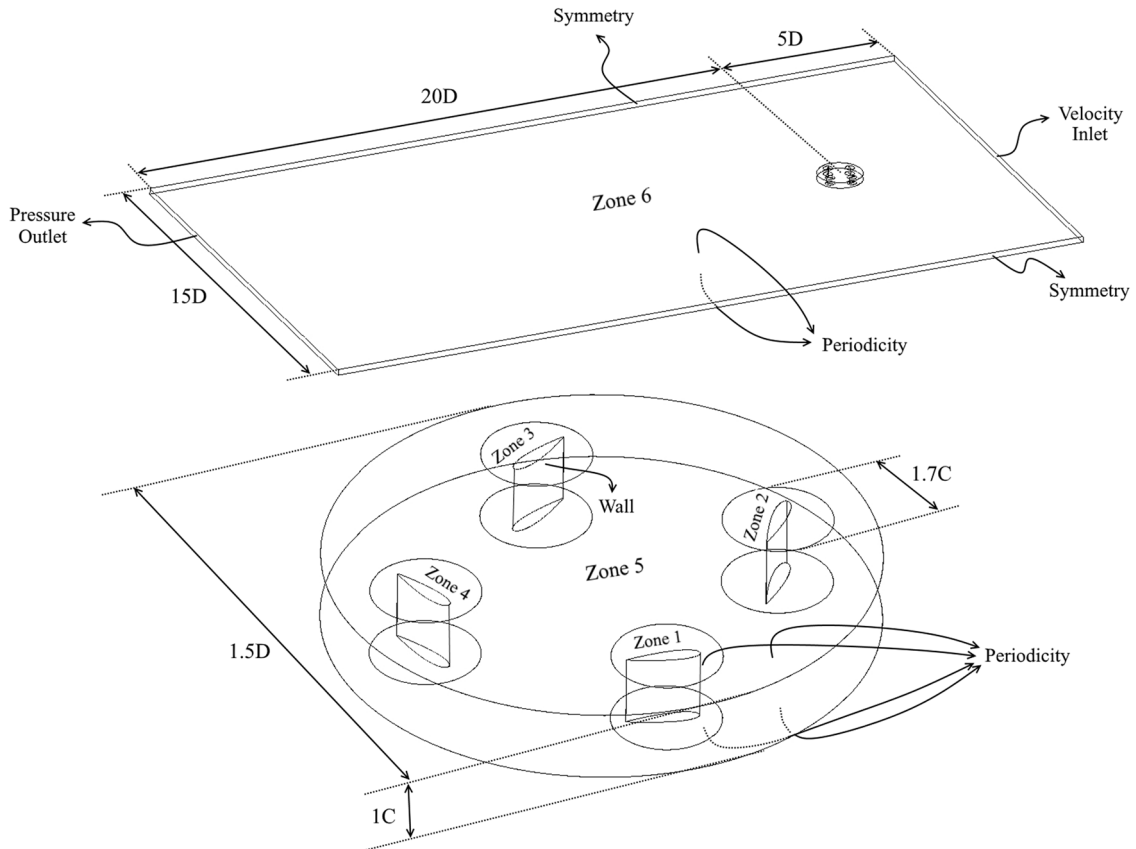


Fig. 6. Computational domain and boundary conditions.

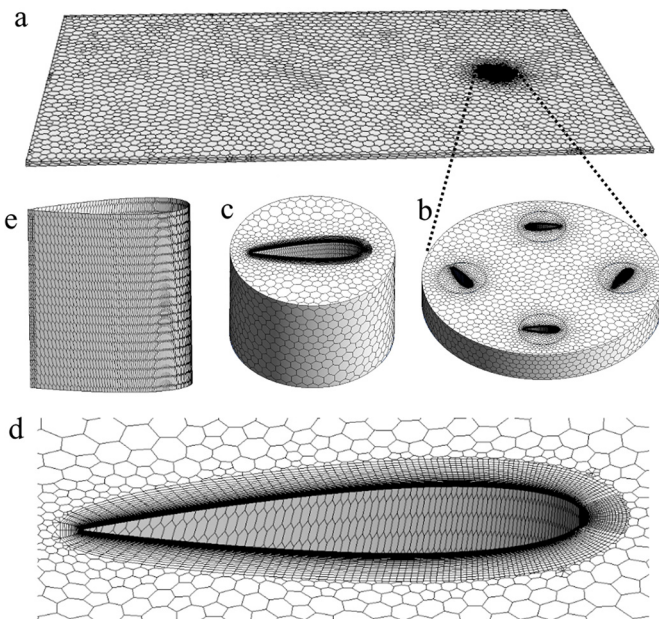


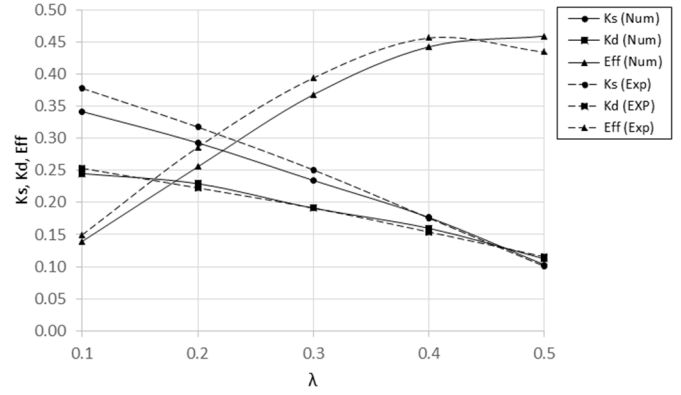
Fig. 7. Computational mesh. (a) Whole solution domain, (b) near-field domain including zones 1, 2, 3, 4 and 5, (c) the mesh of the zone 1, (d) inflation polyhedral layer mesh for near-wall region and boundary layer of the flow, (e) the mesh on blade surface.

Voith-Schneider propeller is examined by comparing with experimental data. Given that the present numerical model is proposed for a VSP (a cycloidal propeller with pure cycloidal motion of the blades) including rectangular blades with symmetric NACA 4-digit profile, the model test carried out by Van Manen [17] was selected as the most appropriate one for validating the numerical method. The Reynolds number of the tests (calculated for the advance coefficient corresponding with the peaks of the efficiency curves) was  $1.4 \times 10^5$ . At this Reynolds number, the scale effect of a cycloidal propeller can be neglected [33]. The specifications of marine cycloidal propeller model tested by Van Manen [17] are given in Table 1.

The numerical model was compared with experimental test for propeller pitch of  $e = 0.6$  at different advance coefficients of  $\lambda = 0.1, 0.2, 0.3, 0.4$  and  $0.5$ . The numerical and experimental results, as well as relative errors, are listed in Table 2. Furthermore, a comparative diagram is illustrated in Figure 8. The average relative errors of thrust coefficient ( $K_s$ ), torque coefficient ( $k_d$ ) and open water efficiency (Eff) are 5.5%, 2.6% and 6.6%, respectively. It should be noted that some part of these errors can be attributed to the lack of full similarity between the numerical simulation and the experimental test, such as the blade tip effects and the variable blade thickness in the model tested. These effects are not included in the presented 2.5D numerical model. However, it can be seen

**Table 1.** Specifications of marine cycloidal propeller model tested by Van Manen [17].

Parameter	Value
Number of blades ( $Z$ )	4
Blade orbit diameter ( $D$ )	0.2 m
Blade span length ( $L$ )	$0.6D = 0.12$ m
Blade chord length ( $c$ )	$0.18D = 0.036$ m
Maximum blade thickness at mid span ( $t$ )	$0.026D = 0.0052$ m
Blade platform	Rectangular
Blade profile	Symmetrical
Blade pitch motion	Pure cycloidal motion
Propeller angular velocity ( $n$ )	6 rps

**Fig. 8.** Comparison between numerical and experimental results for  $e=0.6$ .**Table 2.** Comparison between numerical and experimental results for  $e=0.6$ .

$\lambda$	Numerical			Experimental			Relative error ( $K_s$ )	Relative error ( $K_d$ )	Relative error (Eff)
	$K_s$	$K_d$	Eff	$K_s$	$K_d$	Eff			
0.1	0.341	0.245	0.139	0.378	0.253	0.150	-9.7%	-3.0%	-6.9%
0.2	0.293	0.229	0.255	0.318	0.222	0.286	-7.9%	3.1%	-10.7%
0.3	0.234	0.191	0.368	0.251	0.191	0.394	-6.6%	0.0%	-6.6%
0.4	0.177	0.160	0.442	0.176	0.154	0.456	0.6%	3.8%	-3.0%
0.5	0.103	0.112	0.459	0.100	0.116	0.434	2.6%	-2.9%	5.7%

**Table 3.** Properties of the meshes used for mesh convergence study.

Mesh	Y+ value	Number of inflation layers	Total number of cells in zones 1, 2, 3 and 4	Number of cells in zone 5	Number of cells in zone 6	Total number of cells
Coarse	2	35	449458	6795	2998	459251
Medium	1	45	830174	11236	4917	846327
Fine	0.5	55	1652224	23605	10123	1685952

that there is a good consistency between the numerical results and experimental data. The numerical results presented in Table 2 and Figure 8 relate to the simulations in the finest mesh and time-step of  $dt = T/360$  after performing mesh and time-step convergence study (described below).

A mesh convergence study was carried out based on the Grid Convergence Method (GCI) described in [34], in order to estimate the discretization error and numerical uncertainty. The procedure proposed by [34] is an acceptable and a recommended method that has been evaluated over several hundred CFD cases. For this purpose, numerical simulations were performed for three different meshes (listed in Tab. 3). The mesh refinement

was done uniformly over near-wall and far-field zones. Figure 9 shows the diagrams of mesh independence study for thrust coefficient ( $K_s$ ) and torque coefficients ( $K_d$ ) at  $e=0.6$  and  $\lambda=0.3$ . In addition, the transient values of thrust and torque (calculated for span length of 0.12 m similar to model test) for one revolution of propeller after reaching a periodic state are compared for different meshes in Figure 10. The calculations of discretization error and numerical uncertainty are provided in Table 4. In this table,  $N_1$ ,  $N_2$  and  $N_3$  are the total number of cells, and  $X_1$ ,  $X_2$  and  $X_3$  are performance coefficients of propeller in fine, medium and coarse meshes, respectively.  $r_{21} = (N_1/N_2)^{1/P}$  and  $r_{32} = (N_2/N_3)^{1/P}$  are mesh refinement factors.  $P$  is apparent order.  $X_{ext}^{21}$  is the extrapolated

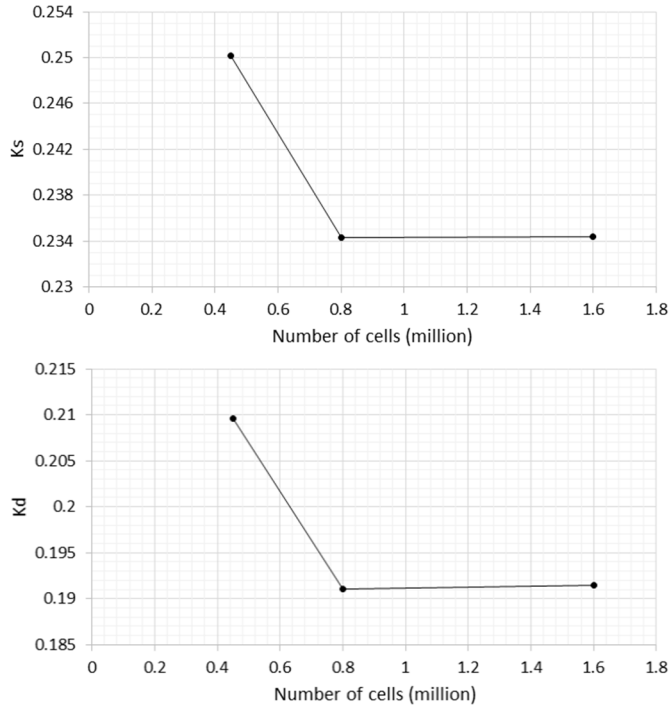


**Fig. 9.** Diagrams of mesh independence study for  $K_s$  and  $K_d$  at  $e = 0.6$  and  $\lambda = 0.3$ .

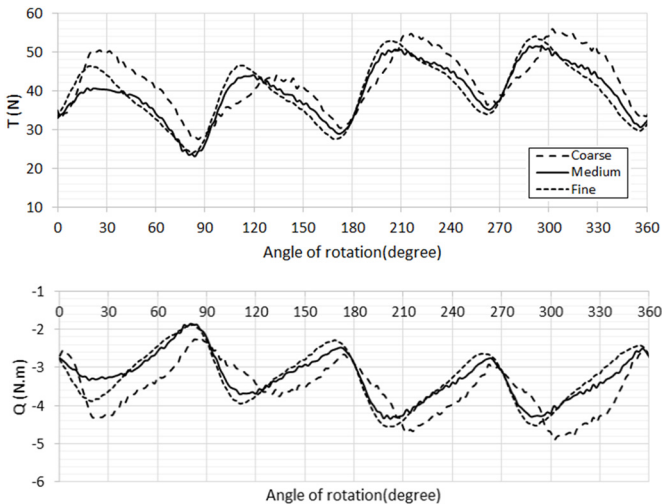


**Fig. 10.** Diagrams of transient thrust and torque for one revolution of propeller for different meshes at  $e = 0.6$  and  $\lambda = 0.3$ .

value of performance coefficient of propeller.  $e_a^{21} = |(X_1 - X_2)/X_1|$  is approximate relative error.  $e_{ext}^{21} = |(X_{ext}^{21} - X_1)/X_{ext}^{21}|$  is extrapolated relative error. According to Table 4, the numerical uncertainties in fine-mesh solution (the fine grid convergence index) for  $K_d$  and  $K_s$  are very low.

After performing the mesh convergence study, the medium mesh was selected to do the main simulations of this study. In order to investigate the independence of

**Table 4.** Calculations of discretization error and numerical uncertainty for  $K_s$  and  $K_d$  at  $e = 0.6$  and  $\lambda = 0.3$ .

Parameter	Thrust coefficient	Torque coefficient
$N_1$	1685952	1685952
$N_2$	846327	846327
$N_3$	459251	459251
$r_{21}$	1.258	1.258
$r_{31}$	1.226	1.226
$X_1$	0.234363	0.191489
$X_2$	0.234296	0.191091
$X_3$	0.250147	0.209570
$p$	26.817	18.805
$X_{ext}^{21}$	0.234364	0.191502
$e_a^{21}$	0.03%	0.21%
$e_{ext}^{21}$	0.0002%	0.0067%
$GCI_{fine}$	0.0003%	0.0084%

solution from temporal discretization, the calculations in medium mesh were performed for two time-steps of  $T/360$  and  $T/720$ , where  $T$  is the period of one revolution of propeller. It was observed that reducing the time-step from  $T/360$  to  $T/720$  had a very little effect on the results of  $K_d$ ,  $K_s$  and Eff. So, all simulations are performed at time step of  $T/360$ , in which the propeller revolves one degree in each time-step of the transient calculations.

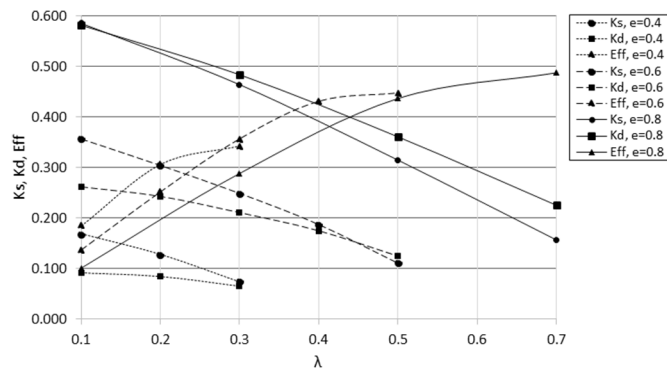
## 5 Results and discussions

The numerical model, which was verified and validated in previous section, is implemented to predict open water characteristics of a model-scale Voith-Schneider propeller including 4 blades with uniform section profile of symmetric NACA 4-digit airfoil. As mentioned before, the effects of the blade tip cannot be included in a 2.5D simulation, so the results of these calculations can only be used for VSP propellers with high aspect ratio (the ratio of blade span length to chord length). The specifications and operating conditions of the VSP models used in this study are provided in Table 5. As listed in this table, the number of blades, diameter and angular velocity of the VSP model are similar to Van Manen's tests [17] used in previous section for validation. The values of 0.024 and 0.042 for  $t/D$  ratio correspond to NACA0012 and NACA0021 section profiles, respectively. It should be noted that all diagrams and numerical results presented in this section are obtained after several revolutions of VSP from initial time, in which the forces on propeller achieve a periodic state in  $360^\circ$  rotation of VSP.

As it is known, when  $\lambda = e$ , the kinematic angle of attack on the blades is zero during rotation of propeller. In this condition, the dynamic lift forces applied on the blades are approximately zero. As a result, the thrust coefficient and open water efficiency of propeller are reduced to about zero at  $\lambda = e$ . In other words, the positive efficiency of a VSP will

**Table 5.** Specifications and operating conditions of VSP models under investigation.

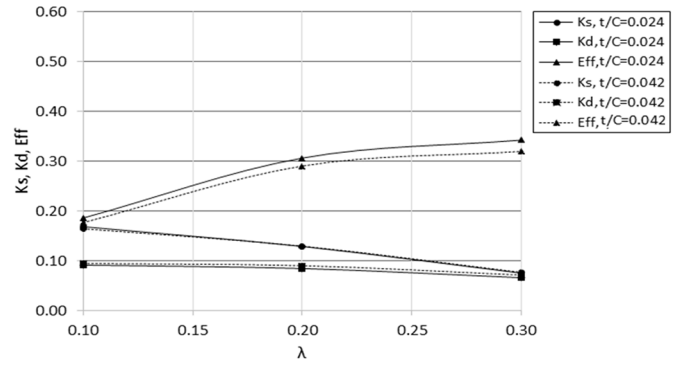
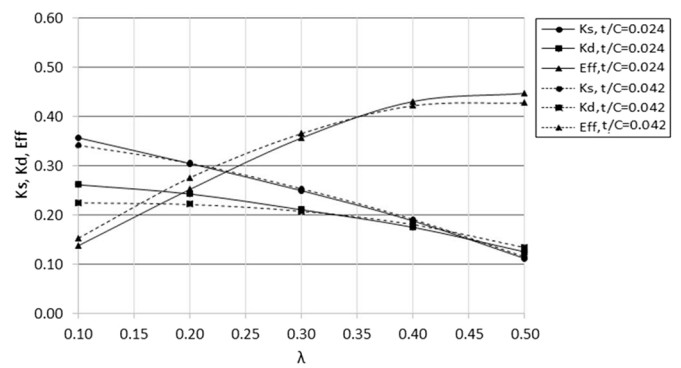
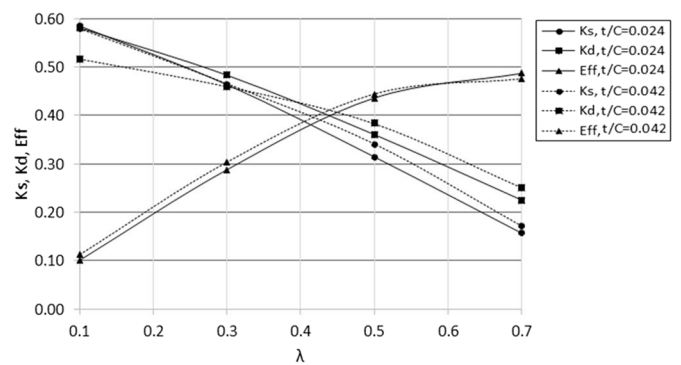
Parameter	Value
Number of blades ( $Z$ )	4
Blade orbit diameter ( $D$ )	0.2 m
Ratio of blade chord to orbit diameter ( $c/D$ )	0.2
Ratio of blade thickness to orbit diameter ( $t/D$ )	0.024, 0.042
Propeller angular velocity ( $n$ )	6 rps
Propeller pitch ( $e$ )	0.4, 0.6, 0.8

**Fig. 11.** Diagram of open water characteristics of VSP at different pitches for  $t/D = 0.024$ .

be nearly up to  $\lambda = e$ . Therefore, here, the performance of VSP for a constant value of  $e$  is calculated for different values of  $\lambda$  from 0.1 to  $(e-0.1)$ .

A diagram of open water characteristics for  $t/D = 0.024$  at different propeller pitches is presented in Figure 11. It can be seen that the maximum efficiency of the VSP is larger for higher propeller pitch. However, at lower advance coefficients, the efficiency decreases by lowering the propeller pitch.

In order to illustrate the effect of blade thickness on performance of a VSP, the diagrams of open water characteristics for two different thicknesses of  $t/D = 0.024$  and  $t/D = 0.042$  are shown in Figures 12–14 for different pitches of 0.4, 0.6 and 0.8, respectively. As shown in these figures, the changes in  $K_s$ ,  $K_d$  is such that, for  $e = 0.6$  and  $e = 0.8$ , the open water efficiency (Eff) increases at first, and then drops, whereas for  $e = 0.4$ , the open water efficiency is decreased at all advance coefficient by increasing blade thickness. What is clear is that the maximum efficiency produced by the VSP decreases with increasing thickness. For a better understanding, the calculated data of efficiency, as well as absolute and percentage of changes in Eff, are provided in Table 6. It can be observed that the average percentage of change in Eff (due to a 75% increase in blade thickness) is only 1.3%, which corresponds to an average absolute change of  $-0.1\%$  ( $-0.001$ ). The average percentage

**Fig. 12.** Diagram of open water characteristics of VSP for two different thicknesses at  $e = 0.4$ .**Fig. 13.** Diagram of open water characteristics of VSP for two different thicknesses at  $e = 0.6$ .**Fig. 14.** Diagram of open water characteristics of VSP for two different thicknesses at  $e = 0.8$ .

of change in maximum Eff is  $-4.5\%$ , which corresponds to an average absolute change of  $-1.8\%$  ( $-0.018$ ). So, the change of blade thickness have little effects on hydrodynamic performance of a VSP.

The velocity contours at the mid-span plane of VSP for  $e = 0.6$  and  $\lambda = 0.4$ , as well as the magnified views of the flow near and inside the boundary layer of a blade, are shown in Figure 15. These contours were calculated for different rotation angles of VSP and one of its blade after 3

**Table 6.** Changes in open water efficiency due to increasing blade thickness.

		Open water efficiency		Absolute change in Eff	Percentage of change in Eff
		$t/c = 0.024$ (NACA0012)	$t/c = 0.042$ (NACA0021)		
$e = 0.4$	$\lambda = 0.1$	18.5%	17.5%	-1.0%	-5.2%
	$\lambda = 0.2$	30.6%	28.9%	-1.7%	-5.4%
	$\lambda = 0.3$	34.2%	31.8%	-2.3%	-6.9%
$e = 0.6$	$\lambda = 0.1$	13.7%	15.2%	1.5%	11.1%
	$\lambda = 0.2$	25.1%	27.5%	2.4%	9.5%
	$\lambda = 0.3$	35.6%	36.5%	0.9%	2.6%
	$\lambda = 0.4$	43.0%	42.2%	-0.8%	-1.9%
	$\lambda = 0.5$	44.6%	42.8%	-1.9%	-4.2%
$e = 0.8$	$\lambda = 0.1$	10.1%	11.2%	1.1%	11.1%
	$\lambda = 0.3$	28.8%	30.3%	1.5%	5.2%
	$\lambda = 0.5$	43.6%	44.4%	0.7%	1.7%
	$\lambda = 0.7$	48.7%	47.5%	-1.2%	-2.5%

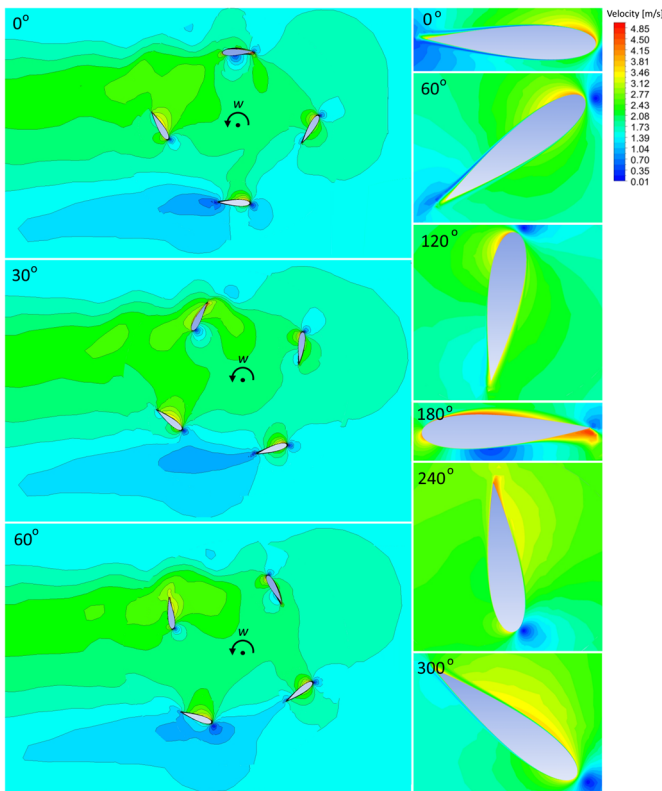


**Fig. 15.** Velocity contours at the mid-span plane at  $e = 0.6$  and  $\lambda = 0.4$  for different rotation angles of the VSP and one of its blade.

revolutions of the propeller. The interactions between four blades of the VSP and the formation of boundary layer on pitching blades at different angles of rotation can be observed in this figure.

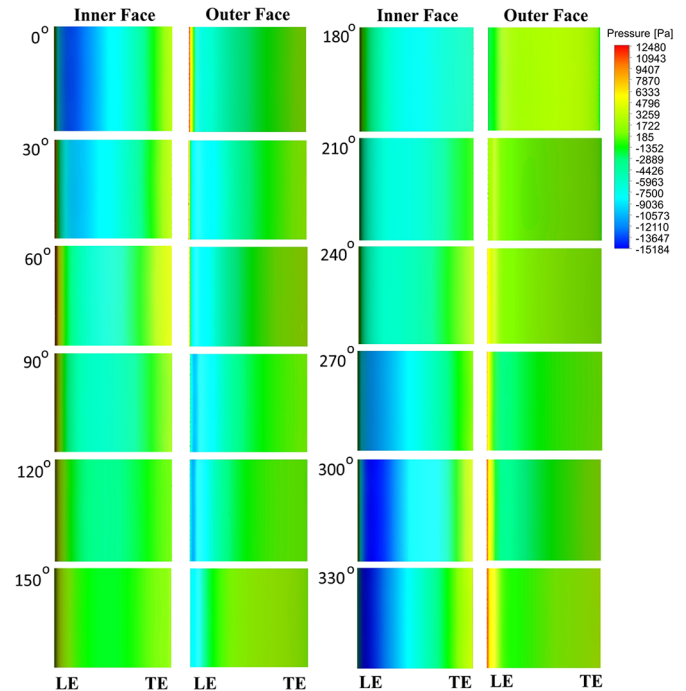


**Fig. 16.** Pressure distributions on the outer and inner faces of a VSP blade at different angular positions for  $e = 0.6$  and  $\lambda = 0.4$ .

The variations of pressure distribution on the outer and inner faces of a blade during propeller rotation are illustrated in Figure 16 for  $e = 0.6$  and  $\lambda = 0.4$ . In this figure, LE and TE represent leading edge and trailing edge, respectively. It can be seen that high pressure differences between inner and outer parts of the blade occur when the blade is pitching in lower part of the VSP (here, at an interval in the range of about  $30^\circ$  before and after zero angle

of rotation). Also, the pressure on the inner side of the blade increases by rotation from  $0^\circ$  to  $180^\circ$  (when the blade is pitching in the fore part of VSP), and decreases again by rotation from  $180^\circ$  to  $360^\circ$  (when the blade is pitching in the aft part of VSP).

## 6 Conclusions

A 2.5D numerical approach based on 3D unsteady RANS equations coupled with SST k- $\omega$  turbulent model was used to predict the open water hydrodynamic performance of a 4-bladed VSP at different propeller pitches and operating conditions. A solution domain with one-chord length in spanwise direction, discretized by a polyhedral mesh, was used for the 2.5D simulations. The presented numerical model was validated against experimental data. According to the numerical results obtained, it can be concluded that 2.5D numerical method presented in this study can be used to accurately predict the open water characteristics of a Voith-Schneider propeller, especially a VSP including blades with high-aspect ratio and uniform section profile. Also, using a polyhedral mesh (as an innovative discretization method), while providing an excellent numerical convergence; can extremely reduce the number of cells and computational time needed for a VSP simulation. In the other hand, using 2.5D simulation, instead of full 3D simulation of VSP, can significantly reduce computational time, while including important 3D effects in spanwise direction. Investigating the effect of the blade thickness on the VSP performance at different pitches, we conclude that the blade thickness has little effects on hydrodynamic performance of a VSP, and the maximum efficiency of VSP decreases with increasing blade thickness at different propeller pitches.

*Acknowledgment.* Numerical computations presented in this study have been performed on the parallel machines of the high performance computing research center (HPCRC) of Amirkabir University of Technology; their supports are gratefully acknowledged.

## References

- [1] S. Mishima, S.A. Kinmas, Application of a numerical optimization technique to the design of cavitating propellers in nonuniform flow, *J. Ship Res.* **41**, 93–107 (1997)
- [2] B. Epps, O. Viquez, C. Chrysostomidis, A method for propeller blade optimization and cavitation inception mitigation, *J. Ship Prod. Des.* **31**, 88–99 (2015)
- [3] J.E. Bartels, D. Jürgens, The Voith Schneider Propeller: Current applications and new developments, Voith Turbo Marine GmbH & Company KG, Alexanderstr **18**, 89522 (2006)
- [4] J. Kirsten, Propeller, Google Patents, 1922
- [5] E. Schneider, Blade wheel, Google Patents, 1928
- [6] VOITH, The Voith GmbH, 2015. <http://voith.com/en/index.html>
- [7] C.J. Henry, A Survey of Cycloidal Propulsion, Davidson Laboratory, Report No. 728, 1959
- [8] K. Taniguchi, Sea trial analysis of the vertical axis propellers. In Fourth Symposium on Naval Hydrodynamics: Propulsion Hydroelasticity, Office of Naval Research and Webb Institute of Naval Architecture, 1962, pp. 27–31
- [9] W.L. Haberman, E.E. Harley, Performance of Vertical Axis (Cycloidal) Propellers Calculated by Taniguchi's Method, Tech report, Report 1564, SR 0090101, Hydromechanics laboratory research and development report, Virginia, 1961
- [10] J.A. Sparenberg, On the Efficiency of a Vertical Axis Propeller, Proceedings of Third Symposium on Naval Hydrodynamics (High Performance Ships) ONR ACR-65, 1960, pp. 45–60
- [11] J.A. Sparenberg, R. de Graaf, On the Optimum one-bladed cycloidal propeller, *J. Eng. Math.* **3**, 1–20 (1969)
- [12] E.C. James, A Small Perturbation Theory for Cycloidal Propellers, PhD Thesis CIT, Pasadena, 1971
- [13] T. Brockett, Hydrodynamic analysis of cycloidal propellers. In Propellers-Shafting Symposium, The Society of Naval Architects and Marine Engineers, 1991
- [14] J. van Manen, T. van Manen, A new way of simulating whale tail propulsion, 21 Symposium on Naval Hydrodynamics, 1996
- [15] B.V. Nakonechny, Experimental Performance of a Six Bladed Vertical Axis Propeller, DTMB Report 1446, 1961
- [16] B.V. Nakonechny, Design of a 9 inch Cycloidal Propeller Model Unit and Some Experimental Results, NSRDC Report 3150, 1975
- [17] J. van Manen, Results of systematic tests with vertical axis propellers, *Int. Shipbuild. Progr.* **13**, 382–398 (1966)
- [18] N.L. Ficken, Conditions for the Maximum Efficiency Operation of Cycloidal Propellers, SNAME Chesapeake Section Paper, 1966
- [19] E. Bjarne, Comparison of a Cycloidal Propeller with Azimuth Thrusters with Regard to Efficiency, Cavitation and Noise, Proceedings of International Conference on Propulsion for Small Craft, RINA, 1982
- [20] N. Bose, P.S.K. Lai, Experimental performance of a trochoidal propeller with high-aspect ratio blades, *J. Mar. Technol.* **26** (1989)
- [21] D. Jürgens, M. Palm, S. Singer, K. Urban, Numerical optimization of the Voith-Schneider Propeller, *ZAMM J. Appl. Math. Mech.* **87**, 698–710 (2007)
- [22] I.S. Hwang, S.J. Kim, Aerodynamic performance enhancement of cycloidal rotor according to blade pivot point movement and preset angle adjustment, *KSAS Int. J.* **9**, 58–63 (2008)
- [23] D. Jürgens, M. Palm, Voith Schneider Propeller-An Efficient Propulsion System for DP Controlled Vessels, Proc. of the Dynamic Positioning Conference, 2009
- [24] M. Palm, D. Jürgens, D. Bendl, Numerical and Experimental Study on Ventilation for Azimuth Thrusters and Cycloidal Propellers, Proc. 2nd Int. Symp. Marine Propulsors smp, 2011
- [25] E. Esmailian, H. Ghassemi, S.A. Heidari, Numerical investigation of the performance of voith schneider propulsion, *Am. J. Mar. Sci.* **2**, 58–62 (2014)
- [26] J. Friesch, Cavitation Studies at the Hamburg Ship Model Basin (HSVA), Hydrodynamic Symposium – Voith Schneider Propulsion, Heidenheim, March, 2006
- [27] D. Jürgens, H.-J. Heinke, Voith Schneider Propeller (VSP)-Investigations of the cavitation behaviour. First International Symposium on Marine Propulsors, SMP, 2009

- [28] J. Rom, High angle of attack aerodynamics, Springer, New York, 1992
- [29] H. Gao, H. Hu, Z.J. Wang, Computational study of unsteady flows around dragonfly and smooth airfoils at low Reynolds numbers, in 46th AIAA aerospace sciences meeting and exhibit, Nevada, Reno, 2008
- [30] F.R. Menter, Two-equation eddy-viscosity turbulence models for engineering applications, *AIAA J.* **32**, 1598–1605 (1994)
- [31] M. Peric, S. Ferguson, The advantage of polyhedral meshes, *Dynamics* **24**, 45 (2005)
- [32] M. Peric, Flow simulation using control volumes of arbitrary polyhedral shape, *ERCFTAC Bulletin*, No. 62, 2004
- [33] A.W. Ruys, A Comparison of Some Published Results of Tests on Vertical Axis Propellers, *International Shipbuilding Progress*, 1966, 13
- [34] P.E. Raad, I.B. Celik, U. Ghia, P.J. Roache, C.J. Freitas, H. Coleman, Procedure for estimation and reporting of uncertainty due to discretization in CFD applications, *J. Fluids Eng.* **130**, 078001 (2008)

**Cite this article as:** M. Bakhtiari, H. Ghassemi, A 2.5D numerical study on open water hydrodynamic performance of a Voith-Schneider propeller, *Mechanics & Industry* **20**, 617 (2019)